# Cascaded Plane Wave Ultrasound for Blood Velocity Vector Imaging in the Carotid Artery

Joosje M. K. de Bakker, *Member, IEEE*, Chris L. de Korte, *Fellow, IEEE*, and Anne E. C. M. Saris, *Member, IEEE*

***Abstract*—Cascaded dual-polarity waves (CDWs) imaging increases the signal-to-noise ratio (SNR) by transmitting trains of pulses with different polarity order, which are combined via decoding afterward. This potentially enables velocity vector imaging (VVI) in more challenging SNR conditions. However, the motion of blood in between the trains will influence the decoding process. In this work, the use of CDW for blood VVI is evaluated for the first time. Dual-angle, plane wave (PW) ultrasound, CDW-coded, and noncoded conventional PW (cPW), was acquired using a 7.8 MHz linear array at a pulse repetition frequency (PRF) of 8 kHz. CDW-channel data were decoded prior to beamforming and cross correlation-based compound speckle tracking for VVI. Simulations of single scatterer motion show a high dependence of amplitude gain on the velocity magnitude and direction for CDW-coded transmissions. Both simulations and experiments of parabolic flow show increased SNRs for CDW imaging. As a result, CDW outperforms cPW VVI in low SNR conditions, based on both bias and standard deviation (SD). Quantitative linear regression and qualitative analyses of simulated realistic carotid artery blood flow show a similar performance of CDW and cPW for high SNR (14 dB) conditions. However, reducing the SNR to 6 dB, results in a root-mean-squared error 2.7× larger for cPW versus CDW, and an $R^2$ of 0.4 versus 0.9. Initial in vivo evaluation of a healthy carotid artery shows increased SNR and more reliable velocity estimates for CDW versus cPW. In conclusion, this work demonstrates that CDW imaging facilitates improved VVI of deeper located carotid arteries.**

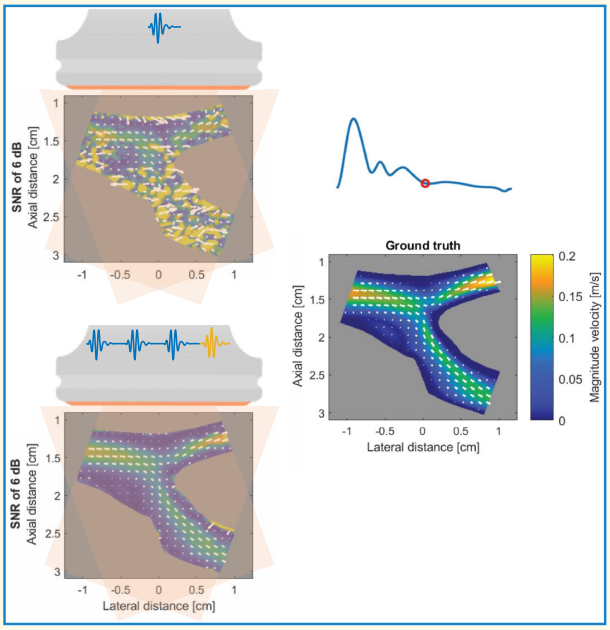


***Index Terms*— Blood flow measurement, blood speckle tracking, carotid artery, cascaded dual-polarity waves (CDWs), coded excitation, plane wave (PW) imaging, velocity vector imaging (VVI).**

## I. Introduction

STROKE is a leading cause of death and major disability in the Western society [1]. Atherosclerosis, i.e., the buildup of plaques in the inner lining of an artery, is one of the primary causes of stroke. The rupture of such a plaque, creates a blood clot which might block an artery supplying the brain with oxygen and nutrients, resulting in a stroke. Complex blood flow patterns in the carotid arteries and the resulting wall shear stresses acting on the vessel wall seem to play a crucial role in the atherosclerotic disease process; from initiation, via progression to the final stage of rupture of plaques [2], [3], [4]. Measuring these complex blood flows could aid in better disease staging, risk assessment, and treatment planning.

Ultrasound is a commonly used technique to examine the vascular tree. However, conventional Doppler-based ultrasound systems cannot measure the complex flow patterns that are considered crucial in the atherosclerotic process, since only the axial velocity component can be measured, i.e., the velocity component along the ultrasound beam direction. As a result, an angle correction is needed to estimate the true velocity vector, which makes the technique highly operator dependent and prone to errors. Besides, when the

Manuscript received 20 December 2023; accepted 13 January 2024. Date of publication 18 January 2024; date of current version 27 February 2024. This work was supported in part by the 2019 Open Technology Program "VORTECS" of the Dutch Research Council (NWO) under Grant 17219 and in part by the Domain Applied and Engineering Sciences (AES). *(Corresponding author: Joosje M. K. de Bakker.)*

This work involved human subjects in its research. Approval of all ethical and experimental procedures and protocols was granted by the Committee on Research Involving Human Subjects Radboud University Medical Center.

Joosje M. K. de Bakker and Anne E. C. M. Saris are with the Medical UltraSound Imaging Center, Department of Medical Imaging, Radboud University Medical Center, 6500 HB Nijmegen, The Netherlands (e-mail: Joosje.deBakker@radboudumc.nl).

Chris L. de Korte is with the Medical UltraSound Imaging Center, Department of Medical Imaging, Radboud University Medical Center, 6500 HB Nijmegen, The Netherlands, and also with the Physics of Fluid Group, Faculty of Science and Technology, University of Twente, 7522 NB Enschede, The Netherlands.

Digital Object Identifier 10.1109/TUFFC.2024.3355712

### *Highlights*

- **This study demonstrates the application of cascaded-wave ultrasound imaging for blood velocity vector imaging in the carotid artery.**
- **Cascaded plane wave transmissions improve signal-to-noise ratio (SNR) and thereby blood velocity vector imaging, especially in low SNR conditions.**
- **Cascaded plane wave ultrasound might be a promising technique for blood velocity vector imaging of deeper located vessels.**

true flow velocity direction is unknown due to complex flow patterns, it becomes difficult, if not impossible, to get an accurate velocity estimate. Two-dimensional velocity vector imaging (VVI), often combined with ultrafast data acquisitions, enables the visualization of complex blood flow patterns within a 2-D imaging plane. Multiple strategies for 2-D angle-independent velocity imaging have been described, such as, speckle tracking [5], [6], vector Doppler [5], [7], directional beamforming [8], [9], and transverse oscillation [8]. All these velocity estimators face similar challenges when it comes to accurately measuring under challenging flow conditions, such as low flows close to the wall, high velocities, high gradients, and out-of-plane motion. The performance of all ultrasound-based VVI techniques, independent of chosen strategy, depends on the (blood) signal-to-noise ratio (SNR) and the ability to remove or suppress the signal from the surrounding tissue (clutter). Compared to conventional imaging, the use of ultrafast ultrasound provides a high continuous temporal resolution. This allows for improved clutter suppression and thereby facilitates the measurement of short-lived events and complex flow patterns [10]. However, the use of plane waves (PWs) or diverging waves, i.e., transmission without focusing, results in a lower contrast and SNR compared to conventional focused line-by-line imaging [11], [12]. Increasing the (blood-)SNR, while using ultrafast ultrasound, is therefore likely to improve the accuracy of the velocity estimates.

In order to increase the blood-SNR, the energy transmitted into the tissue should be increased. Increasing the energy of the transmitted pulse can be done by increasing the length or amplitude of the pulse. However, the design of the transmitted pulse is limited by resolution requirements and safety and/or device restrictions. Coded excitation techniques are used to increase the SNR, without changing the amplitude of the transmitted pulse [13]. Conventional coded excitation techniques make use of the transmission of long modulated signals. The received signals are decoded by a correspondingly designed pulse compression filter [14], [15], [16]. More recently, other coding techniques were described, based on multiple transmit–receive events, with each transmission a different coded excitation. Decoding is performed offline, summing the different transmit–receive events, which overcomes the need of a pulse compression filter [15], [17], [18], [19]. Zhang et al. [15], [20] introduced a cascaded dual-polarity waves (CDWs) imaging scheme, where two trains of pulses are transmitted both with a different polarity order. After transmitting and receiving both trains, they can be decoded by rather simple summation, subtraction, and delaying operations. As a result, the theoretical SNR increase is equal to $10\log_{10}(N)$, with $N$ the number of pulses in a train [15]. The spatiotemporal resolution is not compromised by the use of CDW. The application of CDW has already been shown for tissue motion imaging and power Doppler imaging [20]. However, its application in VVI, where high blood velocities, strong gradients, and complex patterns can result in fast moving and changing (i.e., decorrelating) blood speckle in between two transmitted pulse trains, has not been shown yet.

This article proposes to use CDW for VVI in the carotid artery. A slightly adjusted CDW acquisition and decoding scheme are presented and combined with a previously described VVI method founded on multistep cross correlation based compound speckle tracking [21]. The performance of VVI using CDW acquisitions is compared to the performance using noncoded conventional single pulse plane wave (cPW) acquisitions to study the added value of CDW imaging. First, the effect of blood motion on the CDW-decoding process is evaluated using single scatterer simulations. Second, VVI based on CDW and cPW are evaluated based on simulations and experiments of stationary parabolic flow in a straight tube. Third, simulations of a carotid bifurcation are used to evaluate the technique for more realistic, complex, and clinically relevant flow patterns. Finally, initial in vivo evaluation of VVI using CDW is performed based on the measurement of a healthy carotid artery.

## II. Methods

### *A. Cascaded Waves Imaging Setup*

A L12-5 50 mm transducer (Philips (ATL), Bothell, WA, USA) with a center frequency of 7.8 MHz, attached to a Verasonics Vantage 256 ultrasound system (Verasonics, Kirkland, WA, USA) was used for the measurements. cPW acquisitions consisted of repeated $-20°$ and $+20°$ steered PWs at a pulse repetition frequency (PRF) of 8 kHz. The active aperture (128 out of the 256 elements) between the $-20°$ and $+20°$ PW differed to obtain maximal overlap of both PW beams at the region of interest. For the CDW imaging setup, a train of pulses was transmitted consisting of four cascaded PWs (4-CDW). A train consisted of a combination of positive pulses (+), i.e., normal PWs where the polarity of the initial transition of the transmit waveform is positive, and negative (or inverted) pulses (−) that had a 180° phase shift with respect to the positive pulse. Within a single train, steering angle and thus active aperture were constant. For the subsequent train, only

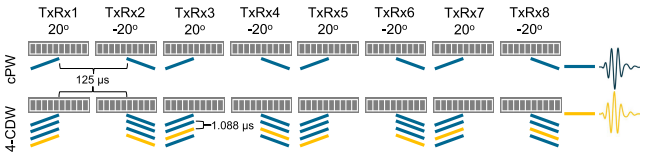


Fig. 1. Dual-angle, conventional PW (top) and 4-CDW (bottom) transmission scheme. Blue rectangles represent a steered PW with a positive polarity and yellow rectangles represent a steered PW with negative polarity. TxRx# stands for the different transmission and receive events. The direction of the rectangles represent their steering angle ($-20°$ or $+20°$).

TABLE I
RELEVANT ACOUSTIC OUTPUT PARAMETERS USING CPW AND 4-CDW

| Parameter | cPW | 4-CDW |
|---|---|---|
| MI | 0.52 | 0.53 |
| $I_{sppa,3}$ (W/cm$^2$) | 37.8 | 11.9 |
| $PII_3$ (J/cm$^2$) | $1.17 \cdot 10^{-5}$ | $4.95 \cdot 10^{-5}$ |
| $I_{spta,3}$ (mW/cm$^2$) | 93 | 396 |

the steering angle changed. The polarity order of the pulses within a train changed after two transmitted trains, i.e., after a $-20°$ transmission followed by a $+20°$ transmission. The polarity order was repeatedly $[+ + + -]$ and $[+ + - +]$. The time in between the start of the different pulses in a single train was 1.088 $\mu$s and the trains were transmitted at a train repetition frequency (TRF) of 8 kHz. Fig. 1 shows an overview of the transmission scheme for both cPW and 4-CDW; this sequence is repeated for the total duration of the acquisition.

The acoustic output of both imaging sequences are within the guideline from the U.S. Food and Drug Administration (FDA) [22]. The relevant acoustic output safety limits are given in Table I. The maximum allowed acquisition duration, limited by probe heating in *still air* and *simulated use* according to the International Electrotechnical Commission [23], was 30 s for cPW and 7 s for 4-CDW. Given the peripheral vessel external use application of the setup and the intention to use ultrafast ultrasound imaging for a maximum duration of 3 s, all safety limits are complied.

To obtain a single pulse PW with an increased SNR, the received RF channel data were decoded prior to beamforming [15], [20]. For the decoding procedure, a combination of two trains (two transmit-receive events) with different polarity order but the same aperture and steering angle were used (i.e., TxRx1 and TxRx3, TxRx2 and TxRx4, in Fig. 1). This decoding process, consisting of repeated summation, subtraction, and delay operations, is visualized schematically for a steering angle of 20° in Fig. 2. The same decoding process was used for the $-20°$ steering angle. Unlike the original implementation of Zhang et al. [15], the summation process was applied one more time to obtain an eightfold increased amplitude, instead of a fourfold when using four pulses in a train. However, at the costs of a reduced PRF. This adopted acquisition scheme is a result of the use of a multiplexed transducer requiring different apertures to create the appropriate overlap of both steering angles at the right imaging depth. Consequently, the theoretical gain in SNR is $10\log_{10}(2N)$, with $N$ the number of pulses in a train. For the example in Fig. 1, where $N = 4$, the theoretical SNR gain will be 9 dB.

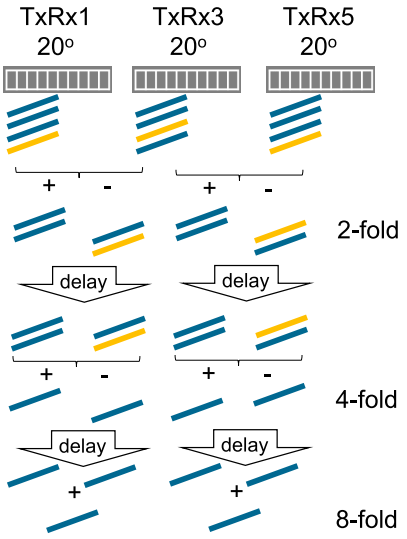


Fig. 2. Schematic illustration of the decoding process for the cascaded PW channel data. Decoding requires two transmit–receive events, or two trains, with different polarity order but same steering angle and aperture. Different summation (+), subtraction (−), and delay operations are executed to obtain an eightfold increased signal amplitude. Note that for combining TxRx3 with TxRx5, the second delay operation is applied to the first (TxRx3) train of that combination, whereas when combining TxRx1 with TxRx3, it is applied to the second train (TxRx3) of that specific combination of TxRx# events.

TABLE II
OVERVIEW OF DIFFERENT TRANSMIT SETTINGS AND BEAMFORMING PARAMETERS

| | |
|---|---|
| **General settings** | |
| Train/pulse repetition frequency | 8 kHz |
| Transmit Voltage Verasonics | 50 V |
| Steering angles | -20/20 degrees |
| Center frequency ($f_c$) | 7.8 MHz |
| Pulse length (cycles at $f_c$) | 3 |
| Sampling frequency ($f_s$) | 31.2 MHz |
| Pitch | 195.3 µm |
| Number of transducer elements | 256 |
| Number of active elements | 128 |
| Depth of elevational focus | 18 mm |
| Apodization window in transmit | Tukey (150 , 30%) |
| Apodization window in receive | Hamming |
| F-number | 0.875 |
| Axial sampling beamforming grid | 12.3 µm |
| Lateral sampling beamforming grid | 51.7 µm |
| **CDW-specific settings** | |
| Interpulse time CDW | 1.088 µs |
| Number of cascaded plane waves in a train | 4 |
| Polarity order of plane waves in train | [+ + + -] and [+ + - +] |

## B. Postprocessing RF Channel Data

After decoding the RF channel data for the CDW image sequence, the data were beamformed using a delay-and-sum technique. Data were beamformed at angulated grids corresponding to the direction of the steered PWs [24]. The same beamforming procedure was applied to reconstruct the cPW data. An overview of the different transmit and beamforming settings is given in Table II.

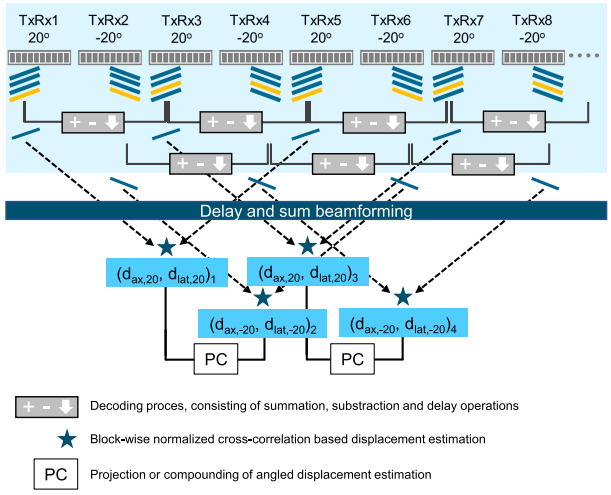


Fig. 3. Schematic illustration of the displacement estimation process. The decoding process, highlighted in light blue, is only applied to the CDW acquisitions. Further processing is equal for CDW and cPW.

### C. Blood Velocity Estimation

For velocity estimation, a dual-angle displacement compounding approach based on (RF-based) speckle tracking was used as described by Saris et al. [21]. Blood velocity vectors were estimated using a normalized cross correlation-based displacement estimation algorithm. Displacements of blood speckles were estimated at an effective PRF of 8000/4 Hz, for data obtained at similar angles (see Fig. 3). The algorithm consisted of two iterations. First, envelope (demodulated RF) data were used to find the coarse speckle displacement. Second, displacement estimates were refined based on RF data. Subsample accuracy was obtained by 2-D cubic interpolation of the cross correlation function [25]. The displacements obtained at $-20°$ and $+20°$ were either projected or compounded to obtain horizontal and vertical displacement estimates. Spatial median filtering of the estimates was performed to remove false estimates and smoothen the velocity fields. Compounding, or triangularization, of solely the axial displacement estimates of both angles was performed when both estimates are of sufficient quality, i.e., when the cross correlation value was larger than 0.6. When this was not the case for one of the angles, the displacement estimate for the remaining angle was projected. When both steering angles were considered of insufficient quality, compounding was performed. Velocity estimation was performed at an effective PRF of 2 kHz, which has two causes. First, inter frame displacements are estimated for data obtained at similar angles, reducing the effective PRF by a factor 2. Second, due to the presence of tissue motion during the transmit–receive events of two pulse-trains, the decoding procedure will be suboptimal, meaning the echoes of those trains will not be perfectly summed and canceled during the decoding process (see Fig. 2). Hereby, the presence of tissue motion effects the appearance of the resulting speckle patterns after beamforming. Consider the received echoes of a single pulse in a train to be represented by a sinusoidal signal $\sin(\alpha)$. In case of no tissue motion, the summation operation for a positive and negative pulse in two subsequent $20°$ trains can then be described by

$$\sin(\alpha) + -\sin(\alpha) \tag{1}$$

which will be equal to zero, resulting in a cancellation of the echoes, as intended. However, in case of tissue motion, causing the second pulse to be shifted by $t$, the summation is described by

$$\sin(\alpha) + -\sin(\alpha + t). \tag{2}$$

Equation (2) describes the suboptimal cancellation of the pulses as a result of tissue motion. In other words, the summation procedure will result in a residual pulse or echo. In case of changing the polarity order, meaning the summation will consist of a first negative pulse and a second positive pulse which is shifted due to tissue motion, the summation can be described by

$$-\sin(\alpha) + \sin(\alpha + t). \tag{3}$$

The residual, noncanceled, pulse of (3) is exactly the opposite of (2). In other words, in the presence of tissue motion, the resulting echo after this summation operation will be inverted depending on the polarity order of the transmitted PWs. As a result, the speckle pattern differs depending on the transmitting order, and the filtering and displacement estimation can only be performed based on decoded data obtained from the same transmit–receive polarity order. Consequently, TxRx1 + TxRx3 and TxRx5 + TxRx7 were handled separately from TxRx3 + TxRx5 and TxRx7 + TxRx9. This reduces the effective PRF with another factor of two, resulting is a final effective PRF for velocity estimation of 2 kHz.

### D. Simulations

For all simulations, Field II pro [26], [27] was used to define an L12-5 transducer, according to the properties described in Table II. The elements of the transducers were subdivided in 10 by 10 mathematical elements, to increase the accuracy of the simulation. A sampling frequency of 250 MHz was used, the simulated channel data were down sampled to $4\times$ the center frequency before further processing. The speed of sound in tissue was assumed to be 1540 m/s and the density 998 kg/m$^3$. For the simulations of parabolic (II-D2) and carotid (II-F) flow a total of 300 scatterers per cubic millimeter were placed inside the lumen to obtain a fully developed speckle pattern. The scatterers had a random amplitude configuration (mean of 0, SD of 1). Band limited white noise ($-10$ dB at 1.4 and 13.0 MHz) was added to scaled simulated channel data, prior to CDW-decoding, to generate the specified effective blood-SNR, i.e., SNR after beamforming for the cPW data. To reduce the computational time, only scatterers inside the $-6$ dB borders of the transmitted PWs were included in the simulation. No vessel wall or surrounding tissues were included in the simulations, so no clutter filtering was applied.

*1) Single Scatterer:* To study the effect of tissue motion or nonzero blood velocities, on the amplitude gain of 4-CDW, first, simple single scatterer simulations were performed. Ultrasound RF channel data was simulated for a single

scatterer (amplitude of one) moving parallel, i.e., beam-to-flow angle (BTFA) of 90°, and perpendicular, i.e., BTFA of 0°, to the transducer footprint. Two −20° pulse trains were simulated at a PRF of 4 kHz, thus 0.25 ms apart and with alternating polarity order of [+ + + −] and [+ + − +]. The starting position of the scatterer was depending on the velocity, such that it will be right in the middle of the transducer at a depth of 18 mm below the surface, in between the two trains. The scatterer was displaced after the first pulse-train, according to its velocity. These simulations were repeated for a range of velocities of 0–5 m/s, with steps of 0.05 m/s. Simulated RF channel data were decoded using the procedure described in Section II-A. As a reference value, cPW data were simulated for the specific situation of a velocity of 0 m/s. The resulting amplitude gain after the decoding process was defined according to

$$\text{Amplitude gain} = |A_{\text{CDW}}|_{x_{\text{cPW,max}}} / \left|A_{\text{cPW,max}}\right| \tag{4}$$

with $|A_{\text{CDW}}|_{x_{\text{cPW,max}}}$ the amplitude of the decoded CDW channel data at the position $x$ of the peak amplitude in the cPW channel data, $|A_{\text{cPW,max}}|$. The amplitude gain was calculated for channel data from the center element of the transducer.

*2) Parabolic Flow:* To study the effect of (suboptimal) decoding on SNR gain and the velocity estimation performance, stationary parabolic flow through a rigid, straight tube was simulated at BTFAs of 90° and 75° for a range of peak velocities ($V_{\text{max}}$): 0.25–3 m/s). The parabolic flow velocity field followed Poiseuille flow and was described by $u = u_c(1 - (r/R)^2)$. Here, $u$ is the velocity at any position $r$ from the centerline, $u_c$ is the maximal velocity, and $R$ is the radius of the tube. The straight tube had a diameter of 10 mm and was centered at 18 mm depth. Channel data were simulated for both noncoded cPW and 4-CDW imaging at a firing PRF of 8 kHz to obtain 100 interframe velocity estimates. Effective blood-SNRs of 5–14 dB were generated by adding noise to the channel data. After decoding the CDW channel data, all data were beamformed (see Section II-B). The SNR of the beamformed CDW data for every peak velocity was compared to the SNR of the cPW data, to determine the SNR gain as a function of peak velocity. The SNR was defined according to $\text{SNR} = 20\log_{10}(\text{rms}_{\text{blood}}/\text{rms}_{\text{noise}})$. With $\text{rms}_{\text{blood}}$ the root mean square (rms) of the signal inside the blood vessel and $\text{rms}_{\text{noise}}$ the rms of the signal outside the blood vessel. An averaged SNR is calculated by averaging the SNR of all individual frames for a certain acquisition protocol and peak velocity.

Velocity estimates were obtained according to the procedure described in Section II-C, using the settings as given in Table III. The performance was evaluated based on the mean horizontal and vertical velocity bias and standard deviation (SD) of 300 estimated velocity profiles. One hundred of these velocity profiles were estimated along the center of the transducer footprint and one hundred 5 mm to the left and right of the center, respectively. The mean velocity bias was calculated according to $m_{\text{bias}} = \text{mean}(m_{m_{\text{est},i}} - \text{GT}_i)$. Here, $\text{GT}_i$ stands for the ground truth at position $i$ across the vessel diameter. $m_{m_{\text{est},i}}$ is the mean velocity estimate at position $i$ of the diameter, based on the 300 velocity profiles. The mean magnitude SD was calculated as the mean of the SD per position across the vessel diameter. The SD per position was calculated based on the 300 velocity profiles. The vertical velocity was separately evaluated from the horizontal velocity component.

TABLE III
OVERVIEW OF DISPLACEMENT ESTIMATION SETTINGS FOR THE PARABOLIC FLOW SIMULATIONS

| Parameter | Blood flow estimation |
|---|---|
| Template size, axial x lateral [mm] | 1.20 x 2.33 (iteration 1)<br>0.60 x 1.20 (iteration 2) |
| Maximal trackable velocity [m/s] | 1.3 x Vmax |
| Median filtering interframe estimates [mm], axial / lateral | 1.0 x 1.0 / 1.0 x 1.0 (iteration 1)<br>0.5 x 0.5 / 0.5 x 0.5 (iteration 2)* |
| Final displacement resolution [mm], vertical x horizontal | 0.1 x 0.1 |

*this step is not performed on the interframe displacements when ensemble averaging takes place afterwards. In this case this filter is only used after ensemble averaging.

## E. Experimental Setup

Experimental performance comparison of 4-CDW and cPW imaging is performed using a straight tube flow setup that ensured parabolic flow [28]. The inner diameter of the tube was 10 mm, and the center was positioned at a depth of 18 mm, similar to the parabolic flow simulations. Blood mimicking fluid (BMF-USA, Shelley Medical Imaging Technologies, London, ON, Canada) was circulated through the setup using a flow-driven gear pump (LifeTec Group, Eindhoven, The Netherlands). Circular symmetric parabolic flow profiles with peak velocities of 0.25, 0.5, and 1 m/s were generated by using a constant flowrate of 0.577 L/min and scaling the peak-velocity-to-PRF ratio accordingly. This constant flow rate was used to avoid generation of air in the BMF at higher flow rates. Two levels of attenuation were created by adding slabs of PDMS with different thickness (Sylgard 184, mixing ratio 10:1, cured at 100 °C for 40 min, speed of sound = 1065 m/s, attenuation = 4.1 dB/cm/MHz) in between the transducer and the tube resulting in an additional attenuation of 8.5 and 11.5 dB. Measurements were performed for both a beam-to-flow angle of 71° and 90°. Further processing and performance evaluation was equal to the parabolic flow simulations as described above. Unlike the simulated data, the experimental beamformed data were clutter filtered using a 60th-order finite impulse response (FIR) clutter filter with a −48 dB cut-off velocity of 0.3 cm/s, with transition region of 1 cm/s (−80 till 0 dB). Clutter filtering was performed at an effective PRF of one fourth of the acquisition PRF, which is equal to the pace of displacement estimation, see Fig. 3. The SNR was determined based on clutter filtered B-mode images. Different from the simulations, only the middle 95% of the vessel diameter was included in bias and SD calculations to avoid boundary effects.

## F. Carotid Bifurcation CFD Model

To further evaluate the performance of 4-CDW imaging, the carotid bifurcation computational fluid dynamics (CFD)

model of Swillens et al. [29] was coupled to Field II pro [26], [27] to simulate RF channel data for more complex, pulsatile, and clinically relevant flow fields. This allows for a detailed assessment of the estimator's performance as estimated velocities can be compared to the actual (ground truth) velocity from CFD. The bifurcation geometry is based on an MRI of a healthy volunteer where an eccentric plaque was artificially added to the internal carotid artery. Scatterers were placed inside the lumen of the carotid artery model and displaced according to the CFD velocity data. To maintain sufficient scatterers inside the vessel, an inlet region was defined just outside the field-of-view. The scatterers in this inlet region where refreshed every 5 ms (every 40 frames) and the scatter configuration in the full lumen was refreshed every 10 ms (every 80 frames) to ensure a constant scatter density throughout the vessel during the entire cardiac cycle. RF channel data were simulated for both the cPW and 4-CDW imaging sequences for a full cardiac cycle of 1 s at a firing PRF of 8 kHz. Noise was added to the simulated channel data to obtain a blood-SNR of 14 to 6 dB, in steps of 2 dB, in the beamformed cPW data, as also explained in Section II-D. Channel data were decoded (for 4-CDW) and beamformed whereafter displacement were estimated at an effective PRF of 2 kHz (see also Section II-C). Ensemble median displacements were calculated using 37 interframe displacements for CDW and 38 interframe displacements for cPW (corresponding to 10 ms) to obtain 100 ensemble averaged velocity estimates throughout the cardiac cycle. An additional threshold was applied to these results. A minimum of 25 interframe displacement estimates within the ensemble, for a specific spatial location, should be obtained with a cross correlation value of 0.6 or higher. In case this condition is met, compounded or projected results will be averaged for the full ensemble. Instead of filtering the second iteration of the interframe displacement estimates, the resulting ensemble averages were filtered using a $0.5 \times 0.5$ mm (axial $\times$ lateral) median filter. This prevents strong transitions between compounded and projected regions.

Performance evaluation of VVI based on 4-CDW and cPW imaging was determined through linear regression between ensemble averaged ground truth and estimated velocities in horizontal and vertical direction. Velocities over the full cardiac cycle and within the overlapping area of the steered PWs ($-20°$ and $20°$) where taken into account for evaluation. Furthermore, a qualitative comparison based on the visual comparison of estimated and ground truth velocity fields is performed for three phases of the heart cycle: peak-systole, end-systole (consisting of a prominent vortex), and diastole.

### G. In Vivo Evaluation

An initial in vivo evaluation has been performed by measuring a healthy, nonstenosed, carotid artery of a 58 year's old volunteer using both cPW and 4-CDW imaging. The local ethics committee (Committee on Research Involving Human Subjects Radboud University Medical Center) waived the need for approval for the collection of this data. Written informed consent was obtained and the data was acquired in accordance with the World Medical Association Declaration of Helsinki. Postprocessing of the acquired data, including beamforming, displacement estimation, and ensemble averaging, was equal to the processing described in Section II-F, for the carotid CFD model. Additionally, clutter filtering was applied using the FIR filter as described in Section II-E, with an adaptive cut-off velocity per ensemble based on the vessel wall motion [21]. To select the reliable velocity estimates, the threshold cross correlation value was reduced to 0.4 for a minimum of 15 interframe estimates within a single ensemble. In case this condition was not met in both steering angles, the final velocity estimate was considered unreliable.

Quantitative comparison of both techniques was based on median [5th–95th percentile] SNR, of clutter filtered data throughout the cardiac cycle. Additionally, the median [5th–95th percentile] normalized cross correlation value, i.e., maximal obtained similarity, for all displacement points and interframe estimates throughout the cardiac cycle was determined. The obtained velocity vector fields where qualitatively compared during two phases in the cardiac cycle, peak systole and late diastole.

## III. Results

### A. Single Scatterer Simulations

The effect of blood velocity on the amplitude gain for 4-CDW-imaging was studied using single scatterer simulations. Fig. 4 shows the amplitude gain in the channel data as a function of the horizontal (BTFA of 90°) and vertical (BTFA of 0°) velocity of a single scatterer. The maximal theoretical amplitude gain of eight is only obtained for a velocity of 0 m/s. For velocities larger than 0 m/s, a repetitive pattern is observed, with an overall gain reduction for larger velocities. Furthermore, almost no gain or even a reduction is observed for certain specific horizontal and vertical velocities. As a result of motion of the scatterer, the path length of the transmitted PW to the scatterer and its travel path back to a single element on the transducer differs between two transmit-receive events. Consequently, the echo from the scatterer ends up at a slightly shifted position in the channel data, leading to a summation process that is only optimal for a velocity of 0 m/s, i.e., no difference in path length. The local minima in the repetitive pattern correspond to a difference in path length equal to $0.5\lambda$, $1.5\lambda$, $2.5\lambda$, etc., causing a 180° phase shift between the trains. This causes cancellation instead of summation of the pulses during the decoding process. The repetitive pattern, and its local minima, is therefore depending on the position of the receiving element, the transmitted center frequency, TRF, the velocity magnitude, the direction of motion, and the position of the scatterer.

### B. Parabolic Flow

The performance of 4-CDW in comparison to cPW imaging in estimating the blood velocity was evaluated using both simulations and experimental measurements of parabolic flow for different SNR conditions. Please note that the noise added to the simulations is scaled according to the cPW data, meaning the effective blood-SNR for CDW imaging is expected to be higher due to the coding/decoding of the pulse trains (see Section II-A). The straight tube experiments were

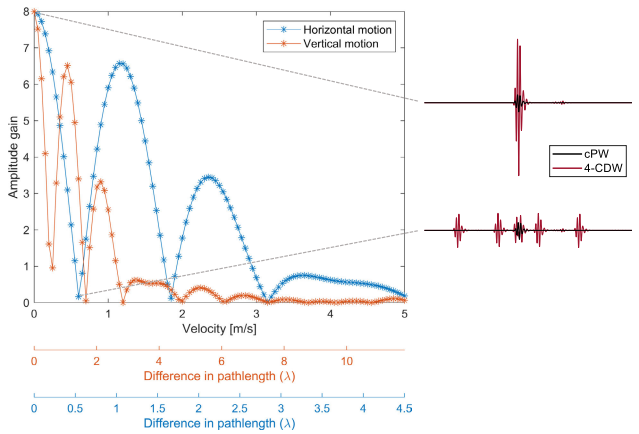


Fig. 4. Amplitude gain as a function of the horizontal (blue) and vertical (orange) velocity of a single scatterer obtained using two trains of 4-CDW with −20° steering angle and a TRF of 4 kHz. The additional $x$-axes show the difference in path length between the first pulses in the two trains. The pulses on the right show the cPW (black) and decoded 4-CDW pulses (red) for a horizontal velocity of 0 and 0.6 m/s.

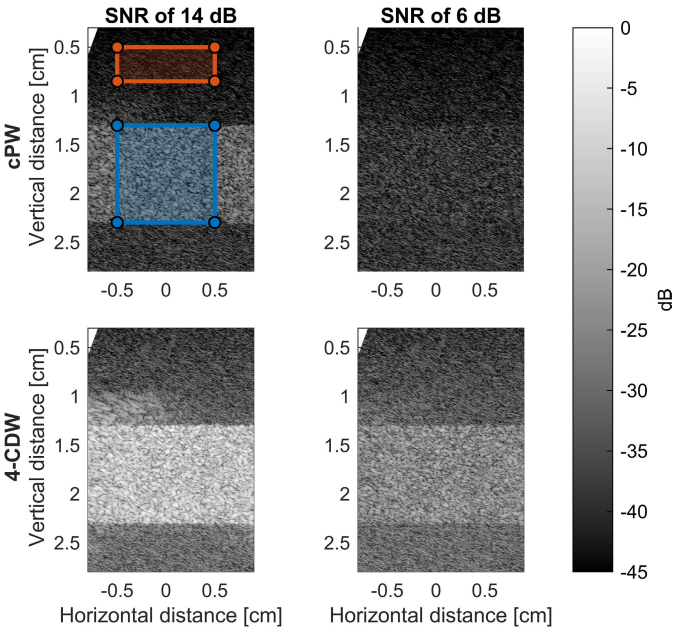


Fig. 5. Simulated B-mode image ($V_{max} = 0.25$ m/s) of cPW (top) and 4-CDW (bottom) with an SNR of 14 (left) and 6 dB (right). The blue region indicated the blood region and orange the noise region used for determining the SNR.

executed without and with two different slabs of PDMS to induce additional attenuation. The resulting blood-SNRs for cPW were, respectively, 16.9, 8.4, and 5.4 dB. Fig. 5 shows the simulated B-mode images of the straight tube vessel phantom for cPW and 4-CDW at an SNR of 14 and 6 dB. The blood and noise regions that are used for the SNR calculation are indicated in the figure. A clear SNR increase is visible for 4-CDW in both SNR conditions. At an SNR of 6 dB, the signal from the blood is not distinguishable from the noise when using cPW, but it still is for 4-CDW. Fig. 6 shows an overview of the blood-SNRs for both cPW and 4-CDW as a function of the peak-velocity of the underlying tissue for both the simulations and experiments. It can be seen that the SNR of 4-CDW is slightly depending on the velocity of the underlying

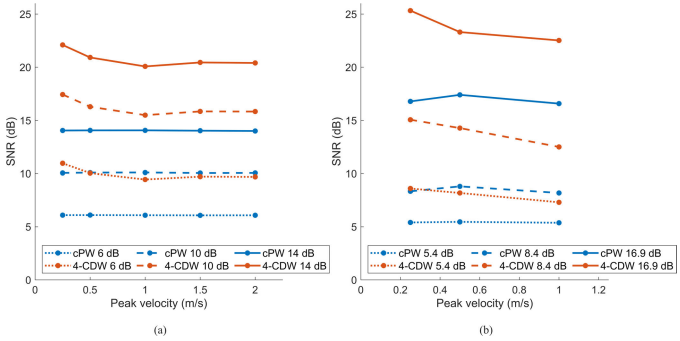


Fig. 6. Blood-SNR as a function of (a) simulated and (b) experimental peak velocity for both cPW (blue) and 4-CDW (orange) for different input SNRs.

tissue. For the simulations, the SNR of cPW is equal for all peak velocities, but the SNR of cPW slightly differs in the experiments. Both simulations and experiments show that the SNR of 4-CDW is always higher compared to the corresponding cPW, regardless of the underlying velocity. Furthermore, the higher the input SNR (SNR of cPW) the higher the gain in SNR for 4-CDW. However, the theoretical gain of 9 dB was never fully reached. For the simulations, a maximum SNR gain of 8.1 dB was observed at a peak velocity of 0.25 m/s and initial cPW-SNR of 14 dB. In comparison, an SNR gain of 4.9 dB was found at an initial cPW-SNR of 6 dB. For a higher peak velocity of 2 m/s, the gain in SNR reduced to 6.4 and 3.6 dB at an initial cPW-SNR of 14 and 6 dB, respectively. This demonstrates the effect of blood velocity on SNR gain. The experimental measurements show the same trends. An SNR gain of 8.5 and 3.2 dB are found at a peak velocity of 0.25 m/s and initial cPW-SNR of 16.9 and 5.4 dB, respectively. This SNR gain reduced to 5.9 and 1.9 dB for a higher peak velocity of 1 m/s.

Fig. 7(a) shows the ground truth (black dashed line), together with the estimated mean velocity ± SD for 4-CDW and cPW at a beam-to-flow-angle of 90° and a peak velocity of 0.25 m/s for the straight tube simulations for blood-SNRs of 14 and 6 dB. The vertical and horizontal velocity component are shown separately. 4-CDW imaging results in a lower bias and SD for both velocity components compared to cPW, which is most apparent at lower SNR. Fig. 7(b) shows the results for a peak velocity of 2 m/s. These results show that increasing the peak velocity increases the bias and SD for both cPW and 4-CDW imaging due to the presence of larger gradients within the velocity field. cPW imaging outperforms 4-CDW imaging at an SNR of 14 dB, especially around the strong gradients at the sides of the parabola. When decreasing the SNR to 6 dB, 4-CDW outperforms cPW based on bias and SD.

Fig. 8 shows an overview of the mean vertical and horizontal velocity bias and SD as a function of SNR, for simulated parabolic flow at a BTFA of 90° and 75° at a peak velocity of 0.25, 1, 2, and 3 m/s. Fig. 9 provides a similar overview for the experiments, for peak velocities of 0.25, 0.5, and 1 m/s. Overall, simulations and experiments show the same results and trends. For simulated and experimental low SNR conditions (SNR $<$ 8 dB), 4-CDW always outperforms cPW based on both bias and SD. The turning point, meaning the SNR at which cPW starts to outperform 4-CDW, depends on the peak

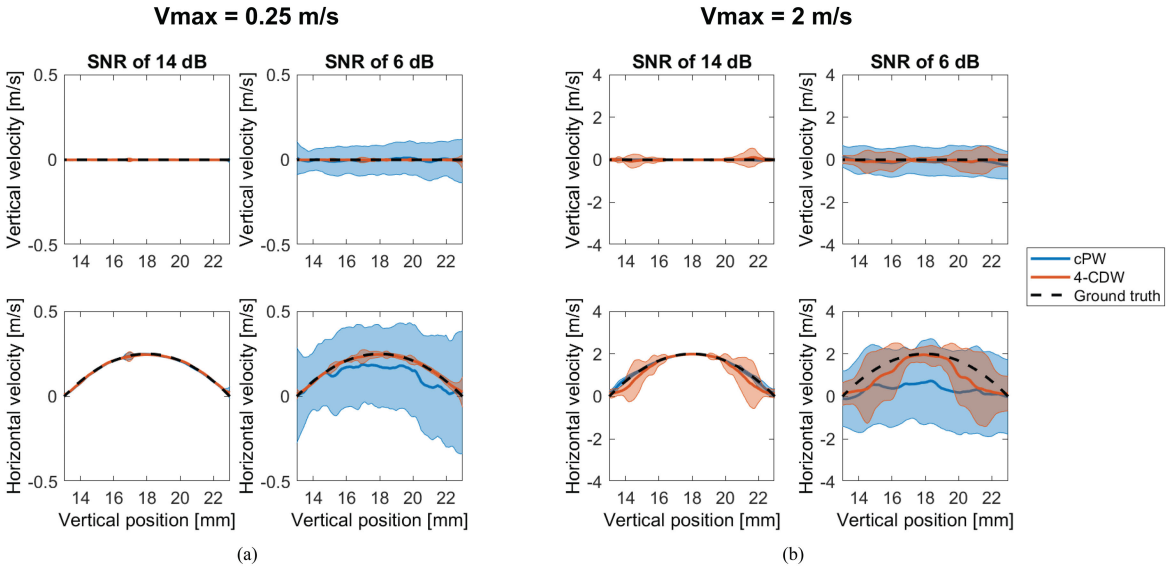


Fig. 7. Field II simulations of parabolic tube flow at a beam-to-flow-angle of 90°. Vertical (top) and horizontal (bottom) velocity components estimated using 4-CDW (orange) and cPW (blue) are compared to the ground truth profiles (black). Results are shown for a peak velocity of (a) 0.25 m/s and (b) 2 m/s with an SNR of 14 dB (left) and 6 dB (right).

TABLE IV
OVERVIEW OF THE REGRESSION ANALYSIS OF BOTH CPW AND 4-CDW IN BOTH THE VERTICAL AND HORIZONTAL DIRECTION FOR SNR CONDITIONS OF 6–14 dB

| | SNR 6 | | | | SNR 8 | | | | SNR 10 | | | | SNR 12 | | | | SNR 14 | | | |
|---|---|---|---|---|---|---|---|---|---|---|---|---|---|---|---|---|---|---|---|---|
| | cPW | | 4-CDW | | cPW | | 4-CDW | | cPW | | 4-CDW | | cPW | | 4-CDW | | cPW | | 4-CDW | |
| | Ver | Hor | Ver | Hor | Ver | Hor | Ver | Hor | Ver | Hor | Ver | Hor | Ver | Hor | Ver | Hor | Ver | Hor | Ver | Hor |
| RMSE (cm/s) | 6.65 | 14.54 | 2.47 | 5.38 | 3.31 | 6.68 | 1.64 | 3.45 | 2.23 | 4.38 | 1.41 | 3.02 | 1.72 | 3.44 | 1.35 | 2.87 | 1.48 | 2.95 | 1.30 | 2.80 |
| $R^2$ (-) | 0.36 | 0.39 | 0.90 | 0.86 | 0.82 | 0.81 | 0.96 | 0.94 | 0.92 | 0.91 | 0.97 | 0.96 | 0.95 | 0.94 | 0.97 | 0.96 | 0.96 | 0.96 | 0.97 | 0.96 |
| Slope (-) | 0.37 | 0.57 | 0.77 | 0.85 | 0.82 | 0.89 | 0.87 | 0.91 | 0.92 | 0.95 | 0.88 | 0.92 | 0.95 | 0.96 | 0.89 | 0.93 | 0.96 | 0.96 | 0.89 | 0.93 |
| Intercept (cm/s) | -0.17 | -0.01 | 0.36 | 0.01 | 0.28 | 0.00 | 0.26 | 0.06 | 0.33 | 0.02 | 0.23 | 0.08 | 0.26 | 0.05 | 0.22 | 0.06 | 0.21 | 0.09 | 0.22 | 0.05 |

velocity and BTFA. For the BTFA of 90°, the turning point varies between 8 and 16.9 dB. For the BTFA of 75°/71°, the turning point lies more at the end of the SNR range (≥12 dB).

### C. Carotid Bifurcation CFD Model

Fig. 10 shows the qualitative comparison between the ground truth velocity fields (from CFD) and the velocity fields obtained with cPW and 4-CDW imaging for the simulated carotid bifurcation flow. VVI was evaluated for three different cardiac phases, peak-systole, end-systole, and diastole, all under blood-SNR conditions of 6 and 14 dB. Given a blood-SNR of 14 dB, cPW imaging and 4-CDW imaging perform very similar for all three phases. The results shows that both methods are able to capture the low-velocity vortex at end-systole as well as the peak velocities at peak-systole. This is also visible in Fig. 11(a), which shows the linear regression analysis for the vertical and horizontal velocity components over the full cardiac cycle. The $R^2$ and root-mean-square error (RMSE) values are very similar for cPW and 4-CDW in both the horizontal and vertical direction, see also Table IV. In case of a lower blood-SNR of 6 dB, 4-CDW clearly outperforms cPW, which can be clearly seen in Fig. 10. Distorted velocity fields are obtained using cPW, while 4-CDW shows velocity fields that still resemble the ground truth. cPW is no longer able to accurately estimate the velocity, especially in the internal carotid artery and in regions closer to the vessel wall. Fig. 11(b) shows the linear regression results for a blood-SNR of 6 dB. It shows that 4-CDW imaging outperforms cPW imaging in both horizontal and vertical direction. The RMSE increases from 1.5 to 6.7 cm/s in vertical direction and from 3.0 to 14.5 cm/s in horizontal direction for cPW imaging when decreasing the SNR from 14 to 6 dB versus 1.3 to 2.5 cm/s and 2.8 to 5.4 cm/s for 4-CDW imaging in vertical and horizontal direction, respectively. An overview of the $R^2$, RMSE, slope, and intercept of the different SNR conditions is given in Table IV. An RMSE of 0 and a $R^2$ of one means that all velocities can be estimated without an error and the velocity is completely described by the ground truth. A slope of one and an intercept of zero, means that the estimated velocity is equal to the velocity of the blood without any bias. In Table IV, it can be seen that the RMSE dramatically increases for cPW compared to 4-CDW for the low SNR conditions, whereas the RMSE is quite similar for an SNR of 12 and 14 dB. The $R^2$ reduces more rapidly for cPW in low SNR conditions, compared to 4-CDW. The slope of the regression analysis is closer to one for the cPW compared to the 4-CDW for a SNR of 10–14 dB. The intercept varies more for the vertical compared to the horizontal velocity magnitude for both cPW and 4-CDW.

### D. In Vivo Evaluation

Fig. 12 shows the qualitative comparison of the velocity vector fields obtained using cPW and 4-CDW acquisitions in a healthy carotid artery. Coherently compounded B-mode

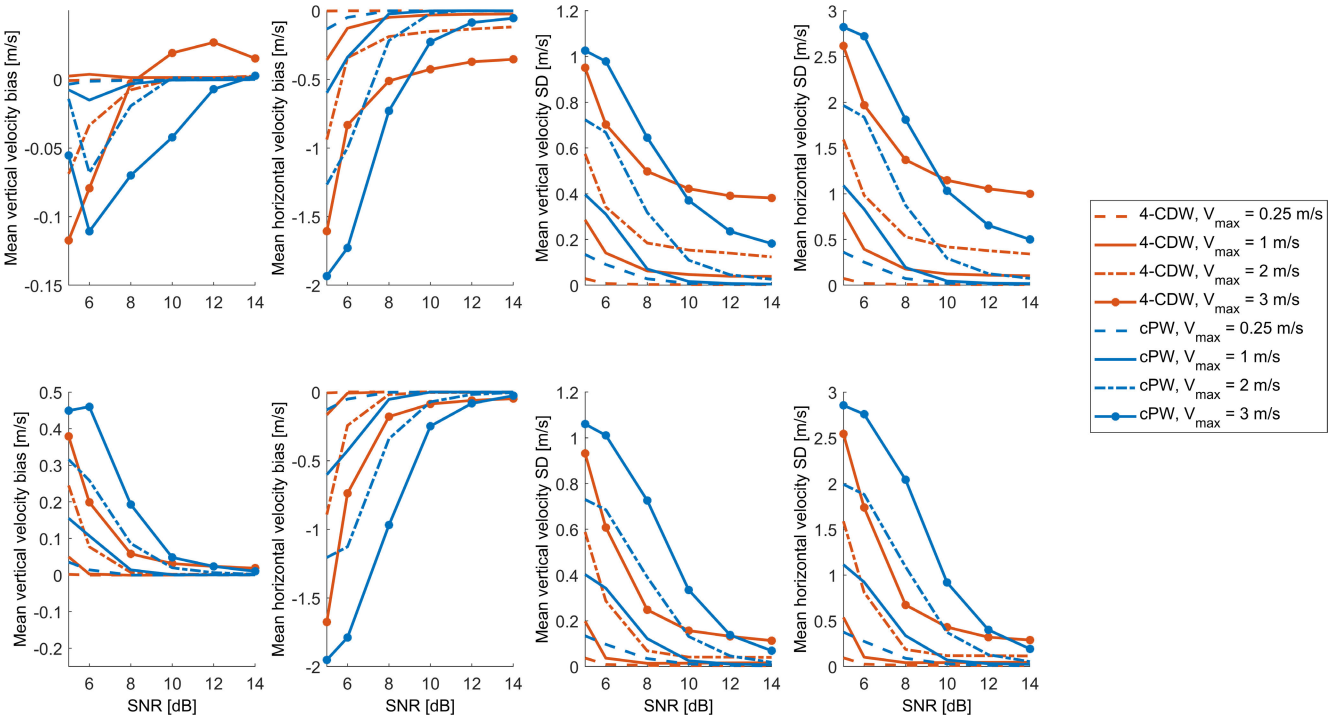


Fig. 8. Mean vertical and horizontal velocity bias (left) and SD (right) for simulated parabolic flow as a function of the SNR. Results for BTFAs of 90° (top) and 75° (bottom) are visualized. Different peak velocities are shown: 0.25 (dashed), 1 (solid), 2 (dash-dotted), and 3 (solid-dot) m/s for both cPW (blue) and 4-CDW (orange) imaging.

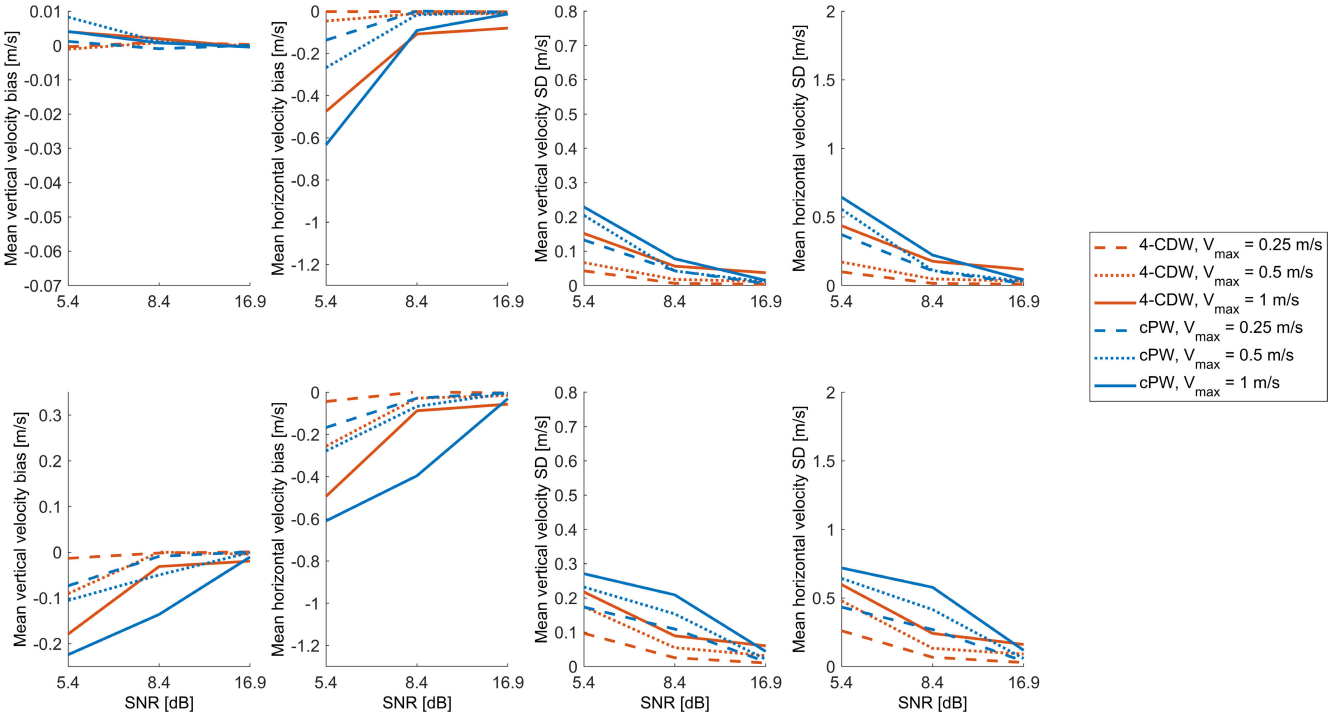


Fig. 9. Mean vertical and horizontal velocity bias (left) and SD (right) for experimental parabolic tube flow as a function of the SNR. Results for BTFAs of 90° (top) and 71° (bottom) are visualized. Different peak velocities are shown: 0.25 (dashed), 0.5 (dotted) and 1 (solid) m/s for both cPW (blue) and 4-CDW (orange) imaging.

images of the carotid bulbus are shown, together with the VVI results during peak-systole and late-diastole, overlaid on the clutter-filtered B-mode images. Unreliable estimates are shown in pink. The median [5th–95th percentile] SNR of cPW was 9.0 [7.9–10.2] dB versus 12.7 [11.2–14.0] dB for 4-CDW imaging. The median [5th–95th percentile] of the cross-correlation values over the full cardiac cycle was 0.36 [0.24–0.64] and 0.57 [0.29–0.82] for cPW and 4-CDW imaging, respectively. As a result, the number of reliable estimates is higher when using 4-CDW imaging, i.e., less

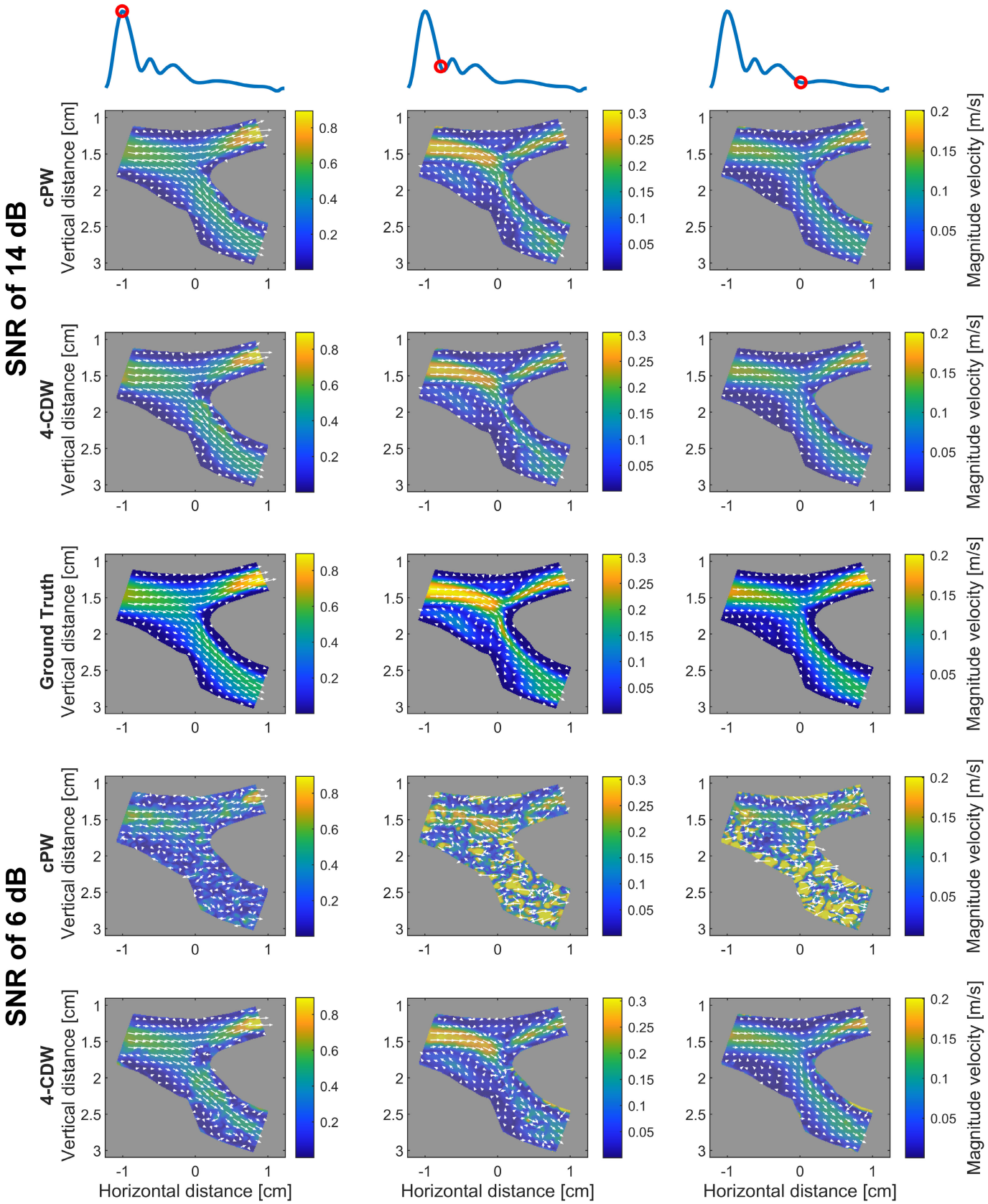


Fig. 10. Ensemble averaged velocity estimates using cPW imaging and 4-CDW imaging compared to the ground truth velocities (middle row) from CFD for three different phases of the heart cycle: peak-systole (left), end-systole (middle), and diastole (right). These positions are also indicated in the doppler trace. SNR conditions of 14 dB (top two rows) and 6 dB (bottom two rows) are shown. The colormap overlay as well as the length of the arrows show the velocity magnitude. The arrows also indicate the direction of the velocity.

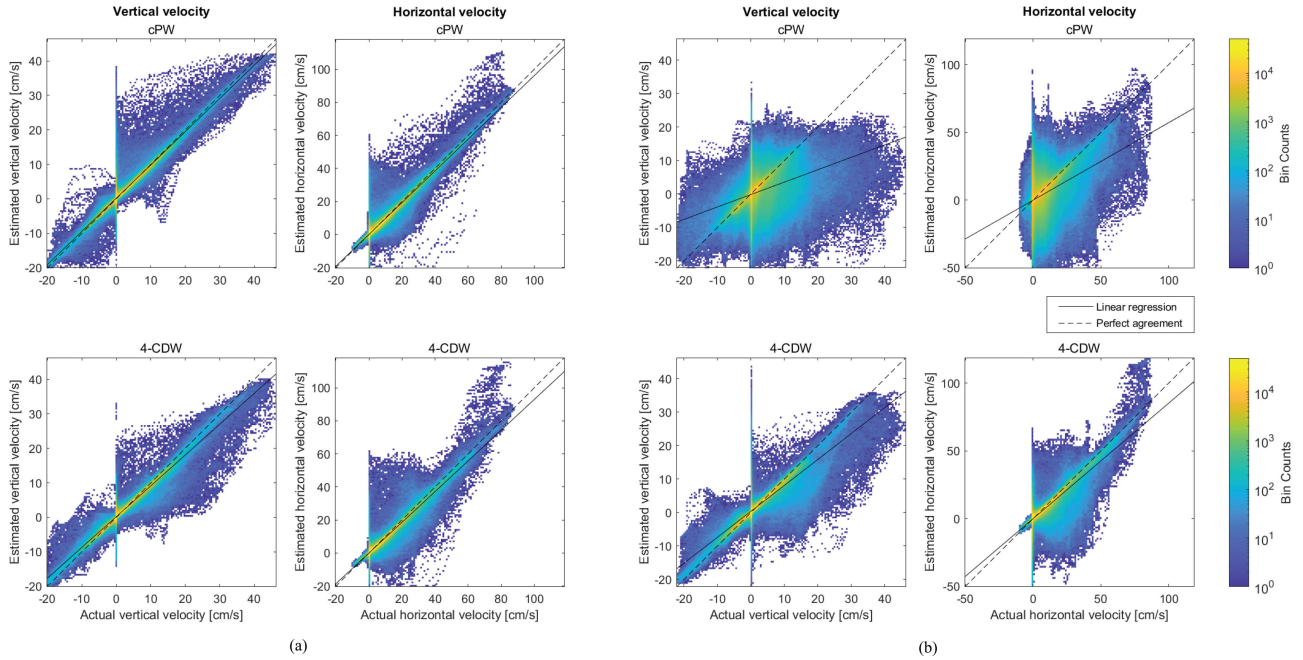


Fig. 11. Estimated versus ground truth velocities for the vertical and horizontal velocity components under different SNR conditions. Linear regression analysis is indicated in the subpanels, showing the resulting linear regression line (dashed black) on top of the 2-D histogram. A perfect regression is indicated by an overlap of the linear regression line with the perfect agreement line (solid black). Results are shown for an SNR of (a) 14 dB and (b) 6 dB.

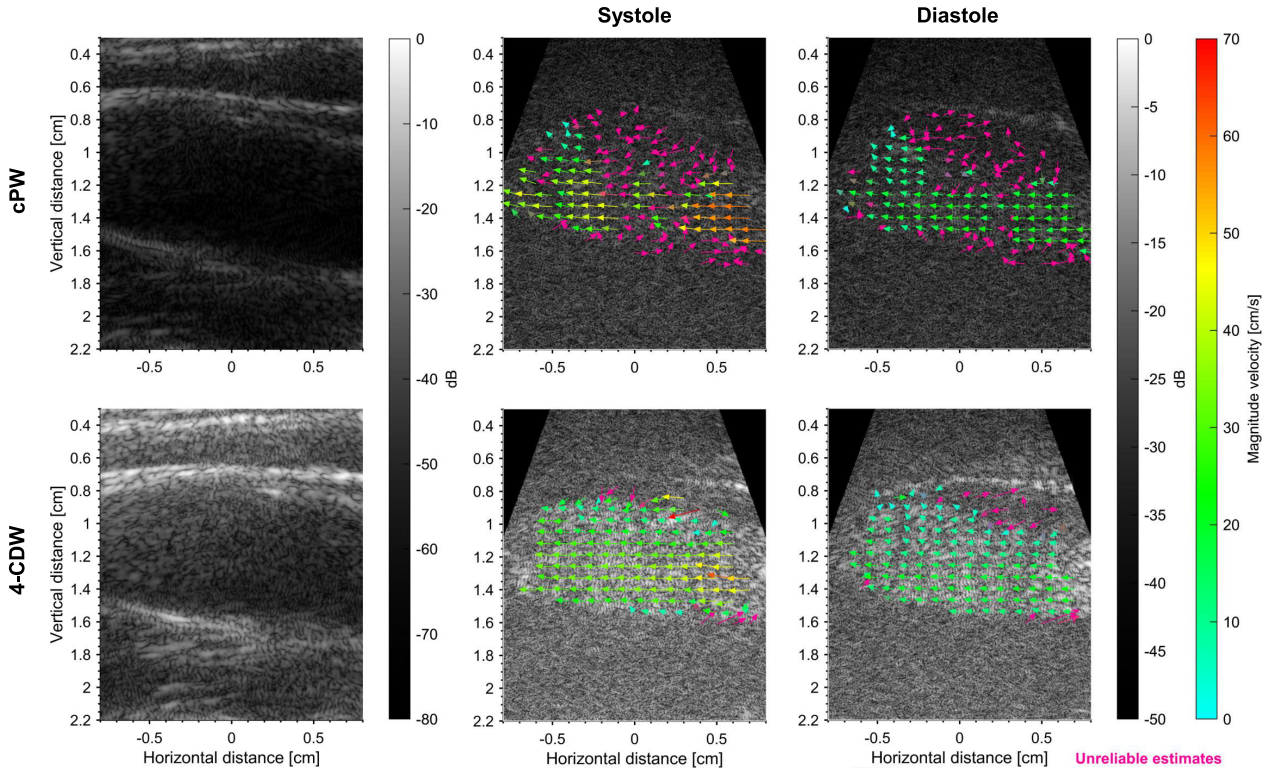


Fig. 12. In vivo results of cPW (top row) and 4-CDW (bottom row) VVI in a healthy carotid artery. The left column shows unfiltered B-mode images (peak-systole). The VVI result are shown on top of clutter filtered B-mode images during peak-systole (middle column) and late-diastole (right column). The arrows indicate the estimated direction of motion. The colors and length of the arrows indicate the velocity magnitude. Unreliable estimates are visualized in pink.

pink arrows. For the unreliable estimates obtained with both methods, the direction and magnitude of the velocity vectors does not seem to be in line with expected in vivo velocity profiles. When only considering the reliable estimates for both cPW and 4-CDW imaging, the results are similar.

## IV. Discussion

This work shows the potential of 4-CDW imaging for VVI using a 2-D cross-correlation-based speckle tracking method. An adjusted acquisition and decoding scheme were presented to allow estimation of 2-D blood velocity vectors. The performance of VVI based on 4-CDW imaging was compared to cPW imaging based on simulations and experiments. The principal finding of this study is, that the use of CDW imaging is feasible for VVI and that it boosts the performance of VVI in low SNR conditions with respect to cPW imaging.

The results of the single scatterer simulations (Fig. 4) show that the 4-CDW-induced amplitude gain strongly depends on the blood motion. In other words, the velocity of blood will influence the alignment of the pulses in two trains and consequently effect addition and cancellation of the pulses in a train, i.e., the decoding process. As explained previously, this imperfect decoding is caused by the difference in the travel path length between two transmit–receive events used for decoding. Theoretically, in case of a pulse with a single frequency, the local minima will occur at $0.5\lambda$, $1.5\lambda$, $2.5\lambda$, etc. However Fig. 4 shows that for larger velocities of the scatterer, the local minima deviate from this theoretical predictions. This can be explained by the fact that the transmitted pulse is composed of a plurality of frequencies, i.e., the bandwidth, and not solely the center frequency. Furthermore, the pulse consist of a limited number of cycles. This effect of amplitude gain depending on the blood velocity can be less clearly seen when imaging a full speckle pattern, see Fig. 5. Depending on the velocity of the underlying tissue, the gain in amplitude and thus the SNR does changes, however, the effects is less strong and less spatially variant as compared to the results shown in Fig. 4. On top of that, Fig. 6 shows that the SNR is always higher for 4-CDW compared to cPW. This is also clearly visible in the B-mode images from Fig. 5. Although the effect of blood velocity on the gain in SNR is less obvious from the effective blood-SNRs, its effect can be seen in the velocity estimates for the straight tube flow simulations (Fig. 7). More accurate 4-CDW estimates are obtained for a peak velocity of 0.25 m/s compared to the peak velocity of 2 m/s, partly as a result of the stronger amplitude gain for relatively low velocities (<0.25 m/s) (Fig. 4). As a result of this amplitude gain for a velocity of 0.25 m/s, 4-CDW outperforms cPW in both simulations (Figs. 7(a) and 8) and experiments (Fig. 9) in both the low and high SNR conditions. On the other hand, an increased bias and SD is found for velocities resulting in a local minima in amplitude gain, e.g., horizontal velocities around 0.6 m/s in Fig. 7(b).

Fig. 6 shows that the gain in SNR for 4-CDW is depending on the input SNR (SNR of cPW), i.e., the higher the input SNR the higher the gain in SNR. This is caused by the fact that for calculating the SNR, the amplitude of the signal including the noise is taken into account, see also Fig. 5. In this way, the definition of SNR is equal for the straight tube simulations and experimental measurements. For high SNR values, the relative contribution of the noise amplitude to the signal power estimate is smaller resulting in a better estimate of the true SNR. When separating the blood signal from the noise signal, which is only possible for the simulated data, the gain in SNR is independent of the input SNR.

In general, for both cPW and 4-CDW imaging, the bias and SD increases for higher velocities due to the larger velocity gradients and consequently decorrelation of the speckle. However, 4-CDW also has to deal with more severe imperfect decoding for higher velocities. This results in increased SD values, as can be observed in Figs. 7–9. In high SNR conditions, the blood signal power obtained with PW imaging is already sufficient for speckle tracking. As a result of the above, cPW outperforms 4-CDW in high SNR and high velocity situations. The similar trend seen in vertical and horizontal velocity SD in Figs. 8 and 9, is a result of mostly compounding the axial displacement estimates to obtain the horizontal and vertical velocity component. The performance evaluation of the parabolic flow simulations and experiments are based on interframe displacements. As a result, the SD is relatively large, but this will reduce in case of using ensemble averaging, which is an often used technique in VVI.

Previously, it was shown that the cPW displacement estimator is a robust estimator in parabolic flow conditions [21]. However, no extended evaluation was performed under more challenging SNR conditions. This work shows that with the use of 4-CDW imaging, the estimator is still able to estimate parabolic, but also more complex flow under low SNR conditions. For the simulations, no vessel wall or surrounding tissue (motion) was taken into account. Clutter filtering was therefore not applied to the beamformed RF data. The presented results therefore reflect the performance of the estimators under ideal conditions. A clutter filter was applied to the experimental straight tube data to suppress the signals from the vessel wall. Comparing the parabolic flow simulations to the experiments, similar effects of velocity and SNR on the velocity estimation performance (bias and SD) were seen.

The carotid bifurcation simulations show that also in more complex, clinically relevant flow situations, 4-CDW outperforms cPW imaging in the low SNR conditions. At an SNR of 6 dB, the RMSE is 2.7× larger for cPW compared to 4-CDW in both the vertical and horizontal direction and the $R^2$ reduces from 0.9 to 0.4. However, contradictory to the parabolic flow situations, 4-CDW and cPW perform very similar for an SNR of 14 dB. Although for certain spatial positions, inadequate decoding of CDW due to the underlying blood velocity results in a larger SD of the interframe displacement estimates, the effect on the final ensemble averaged velocity estimation is limited. Most inaccurate velocity estimates are obtained at the borders of the lumen area, i.e., close to the vessel wall (not simulated). Here, the ground truth velocity is approximating zero, however, due to the kernel size and the surrounding tissue containing only noise, the cross-correlation-based velocity estimator has difficulty estimating this velocity. This can also be seen from Fig. 11, where the largest spread in estimates is concentrated at an actual, or ground truth, velocity of zero.

The initial in vivo evaluation presented in Fig. 12 shows an increased SNR and more reliable velocity estimates for 4-CDW versus cPW imaging. The results are in line with

the results from simulations and experiments, and strongly indicate the use of CDW imaging for in vivo use, where often cPW faces limited SNR conditions and, as a result, less reliable or even unreliable velocity estimates.

The use of 4-CDW acquisitions and the proposed decoding process results in a reduced effective PRF for velocity estimation. The reduced effective PRF makes the technique more prone to decorrelation effects in case of relatively high velocities. When using cPW, displacement estimation could be performed at a PRF of 4 kHz. This effect was tested for the parabolic flow simulations, but showed little effect on the bias and SD. Due to the reduced interframe displacement, the lower velocities are less accurately estimated (subsample displacement), whereas the higher velocities are estimated slightly better. To discard this effect, the performance of cPW and 4-CDW-based velocity estimates was compared based on the same processing (Fig. 3). In order to increase the PRF for displacement estimation of 4-CDW, two steering angles could be transmitted in a single train. After decoding, the two steering angles are separated and two PWs, with increased SNR and different steering angles are obtained, as was also done by Zhang et al. [15]. In order to combine this with the compound speckle tracking method, a nonmultiplexed transducer with a sufficiently large footprint, adequate pitch, 192–256 elements, and optimal center frequency (7–8 MHz) is required. The choice of only four cascaded waves in a train was in this research limited by the IEC approved temperature rise of the probe surface on tissue and in air [23]. The obtained amplitude gain could therefore not be increased more, without further decreasing the effective PRF.

To make cascaded PW imaging less susceptible to motion, future work will focus on correcting for the imperfect decoding as a result of blood motion. Similar motion compensation strategies as used for phase aberration correction [30], synthetic transmit aperture imaging [31], and spatial encoded imaging [32] could be applied to CDW-based velocity imaging. Such a correction will result not only in more amplitude gain but also less blurring of the image. This is especially important for lower BTFA as this means that the axial movement is larger and axial motion results in more imperfect decoding due to a faster changing path length, see Fig. 4. Another solution to reduce the imperfect decoding is increasing the TRF. However, this will result in heating problems and is therefore not a solution for in vivo measurements.

## V. Conclusion

In summary, it is shown that the general reduced signal power of cPW can be boosted by 4-CDW imaging and that 4-CDW imaging is able to accurately visualize and quantify parabolic and complex clinically relevant velocity fields accurately. Most importantly, in low SNR conditions, where conventional, noncoded PW imaging fails to enable accurate VVI, CDW imaging enables this by increasing the effective SNR. As a result, 4-CDW imaging for VVI is especially useful in challenging in vivo conditions, such as deeper located vessels and presence of strong attenuating tissue layers. Further research will focus on extended in vivo evaluation and compensation of the imperfect decoding in order to further increase the potential of this technique.

## References


[1] M. Katan and A. Luft, "Global burden of stroke," *Semin Neurol.*, vol. 38, no. 2, pp. 208–211, 2018, doi: 10.1055/s-0038-1649503. [Online]. Available: https://www.ncbi.nlm.nih.gov/pubmed/29791947

[2] C. M. Warboys, N. Amini, A. D. Luca, and P. C. Evans, "The role of blood flow in determining the sites of atherosclerotic plaques," *F Med. Rep.*, vol. 3, p. 5, Mar. 2011. [Online]. Available: https://www.ncbi.nlm.nih.gov/pubmed/21654925

[3] A. M. Malek, S. L. Alper, and S. Izumo, "Hemodynamic shear stress and its role in atherosclerosis," *JAMA*, vol. 282, pp. 2035–2042, Dec. 1999.

[4] C. Slager et al., "The role of shear stress in the destabilization of vulnerable plaques and related therapeutic implications," *Nature Clin. Pract. Cardiovascular Med.*, vol. 2, no. 9, pp. 456–464, Sep. 2005, doi: 10.1038/ncpcardio0298. [Online]. Available: https://www.ncbi.nlm.nih.gov/pubmed/16265586

[5] S. Fadnes, I. K. Ekroll, S. A. Nyrnes, H. Torp, and L. Lovstakken, "Robust angle-independent blood velocity estimation based on dual-angle plane wave imaging," *IEEE Trans. Ultrason., Ferroelectr., Freq. Control*, vol. 62, no. 10, pp. 1757–1767, Oct. 2015, doi: 10.1109/TUFFC.2015.007108. [Online]. Available: https://www.ncbi.nlm.nih.gov/pubmed/26470038

[6] G. E. Trahey, S. M. Hubbard, and O. T. von Ramm, "Angle independent ultrasonic blood flow detection by frame-to-frame correlation of B-mode images," *Ultrasonics*, vol. 26, no. 5, pp. 271–276, Sep. 1988, doi: 10.1016/0041-624x(88)90016-9. [Online]. Available: https://www.ncbi.nlm.nih.gov/pubmed/2970144

[7] B. Dunmire, K. Beach, K.-H. Labs, M. Plett, and D. S. Strandness Jr., "Cross-beam vector Doppler ultrasound for angle-independent velocity measurements," *Ultrasound Med. Biol.*, vol. 26, pp. 1213–1235, 2000.

[8] J. Jensen, C. A. Villagómez Hoyos, M. B. Stuart, C. Ewertsen, M. B. Nielsen, and J. A. Jensen, "Fast plane wave 2-D vector flow imaging using transverse oscillation and directional beamforming," *IEEE Trans. Ultrason., Ferroelectr., Freq. Control*, vol. 64, no. 7, pp. 1050–1062, Jul. 2017, doi: 10.1109/TUFFC.2017.2693403. [Online]. Available: https://www.ncbi.nlm.nih.gov/pubmed/28422656

[9] J. A. Jensen, "Directional velocity estimation using focusing along the flow direction. I: Theory and simulation," *IEEE Trans. Ultrason., Ferroelectr., Freq. Control*, vol. 50, no. 7, pp. 857–872, Jul. 2003, doi: 10.1109/TUFFC.2003.1214505. [Online]. Available: https://www.ncbi.nlm.nih.gov/pubmed/12894919

[10] S. Fadnes, S. Bjærum, H. Torp, and L. Lovstakken, "Clutter filtering influence on blood velocity estimation using speckle tracking," *IEEE Trans. Ultrason., Ferroelectr., Freq. Control*, vol. 62, no. 12, pp. 2079–2091, Dec. 2015, doi: 10.1109/TUFFC.2015.007247. [Online]. Available: https://www.ncbi.nlm.nih.gov/pubmed/26670849

[11] G. Montaldo, M. Tanter, J. Bercoff, N. Benech, and M. Fink, "Coherent plane-wave compounding for very high frame rate ultrasonography and transient elastography," *IEEE Trans. Ultrason., Ferroelectr., Freq. Control*, vol. 56, no. 3, pp. 489–506, Mar. 2009, doi: 10.1109/TUFFC.2009.1067. [Online]. Available: https://www.ncbi.nlm.nih.gov/pubmed/19411209

[12] M. Tanter and M. Fink, "Ultrafast imaging in biomedical ultrasound," *IEEE Trans. Ultrason., Ferroelectr., Freq. Control*, vol. 61, no. 1, pp. 102–119, Jan. 2014, doi: 10.1109/TUFFC.2014.6689779. [Online]. Available: https://www.ncbi.nlm.nih.gov/pubmed/24402899

[13] S. I. Nikolov and J. A. Jensen, "Comparison between different encoding schemes for synthetic aperture imaging," *Proc. SPIE*, vol. 4687, pp. 1–12, Jan. 2002.

[14] T. Misaridis and J. A. Jensen, "Use of modulated excitation signals in medical ultrasound. Part III: High frame rate imaging," *IEEE Trans. Ultrason., Ferroelectr., Freq. Control*, vol. 52, no. 2, pp. 208–219, Feb. 2005.

[15] Y. Zhang, Y. Guo, and W.-N. Lee, "Ultrafast ultrasound imaging with cascaded dual-polarity waves," *IEEE Trans. Med. Imag.*, vol. 37, no. 4, pp. 906–917, Apr. 2018, doi: 10.1109/TMI.2017.2781261. [Online]. Available: https://www.ncbi.nlm.nih.gov/pubmed/29610070

[16] V. Behar and D. Adam, "Parameter optimization of pulse compression in ultrasound imaging systems with coded excitation," *Ultrasonics*, vol. 42, no. 10, pp. 1101–1109, Aug. 2004, doi: 10.1016/j.ultras.2004.02.020. [Online]. Available: https://www.ncbi.nlm.nih.gov/pubmed/15234172

[17] E. Tiran et al., "Multiplane wave imaging increases signal-to-noise ratio in ultrafast ultrasound imaging," *Phys. Med. Biol.*, vol. 60, no. 21, pp. 8549–8566, Nov. 2015, doi: 10.1088/0031-9155/60/21/8549. [Online]. Available: https://www.ncbi.nlm.nih.gov/pubmed/26487501

[18] Y. R. Chen, X. Q. Shi, L. X. Qian, and J. W. Luo, "S-sequence encoded multiplane wave imaging: Phantom and in-vivo validation," in *Proc. IEEE Int. Ultrason. Symp. (IUS)*, Oct. 2018, pp. 1–4.

[19] P. Gong, M. C. Kolios, and Y. Xu, "Delay-encoded transmission and image reconstruction method in synthetic transmit aperture imaging," *IEEE Trans. Ultrason., Ferroelectr., Freq. Control*, vol. 62, no. 10, pp. 1745–1756, Oct. 2015, doi: 10.1109/TUFFC.2015.007005.

[20] Y. Zhang, H. Li, and W.-N. Lee, "Imaging heart dynamics with ultrafast cascaded-wave ultrasound," *IEEE Trans. Ultrason., Ferroelectr., Freq. Control*, vol. 66, no. 9, pp. 1465–1479, Sep. 2019, doi: 10.1109/TUFFC.2019.2925282. [Online]. Available: https://www.ncbi.nlm.nih.gov/pubmed/31251182

[21] A. E. C. M. Saris, H. H. G. Hansen, S. Fekkes, J. Menssen, M. M. Nillesen, and C. L. de Korte, "In vivo blood velocity vector imaging using adaptive velocity compounding in the carotid artery bifurcation," *Ultrasound Med. Biol.*, vol. 45, no. 7, pp. 1691–1707, Jul. 2019, doi: 10.1016/j.ultrasmedbio.2019.03.008. [Online]. Available: https://www.ncbi.nlm.nih.gov/pubmed/31079874

[22] US Food and Drug Administration, *Marketing Clearance of Diagnostic Ultrasound Systems and Transducers*, Food Drug Admin., Center Devices Radiol. Health, Silver Spring, MD, USA, 2023. [Online]. Available: https://www.fda.gov/regulatory-information/search-fda-guidance-/marketing-clearance-diagnostic-ultrasound-systems-and-transducers

[23] Commission International Electrotechnical, *Medical Electrical Equipment—Part 2–37: Particular Requirements for the Basic Safety and Essential Performance of Ultrasonic Medical Diagnostic and Monitoring Equipment*, Int. Electrotech. Commission, Geneva, Switzerland, 2015. [Online]. Available: https://webstore.iec.ch/publication/22634

[24] A. E. C. M. Saris, H. H. G. Hansen, S. Fekkes, M. M. Nillesen, M. C. M. Rutten, and C. L. de Korte, "A comparison between compounding techniques using large beam-steered plane wave imaging for blood vector velocity imaging in a carotid artery model," *IEEE Trans. Ultrason., Ferroelectr., Freq. Control*, vol. 63, no. 11, pp. 1758–1771, Nov. 2016, doi: 10.1109/TUFFC.2016.2606565.

[25] A. Saris, S. Fekkes, M. Nillesen, H. Hansen, and C. de Korte, "A PSF-shape-based beamforming strategy for robust 2D motion estimation in ultrafast data," *Appl. Sci.*, vol. 8, no. 3, p. 429, 2018, doi: 10.3390/app8030429.

[26] J. Jensen, "Field: A program for simulating ultrasound systems," *Med. Biol. Eng. Comput.*, vol. 34, pp. 351–353, Jan. 1996.

[27] J. A. Jensen and N. B. Svendsen, "Calculation of pressure fields from arbitrarily shaped, apodized, and excited ultrasound transducers," *IEEE Trans. Ultrason., Ferroelectr., Freq. Control*, vol. 39, no. 2, pp. 262–267, Mar. 1992, doi: 10.1109/58.139123. [Online]. Available: https://www.ncbi.nlm.nih.gov/pubmed/18263145

[28] S. Fekkes, A. E. C. M. Saris, M. M. Nillesen, J. Menssen, H. H. G. Hansen, and C. L. de Korte, "Simultaneous vascular strain and blood vector velocity imaging using high-frequency versus conventional-frequency plane wave ultrasound: A phantom study," *IEEE Trans. Ultrason., Ferroelectr., Freq. Control*, vol. 65, no. 7, pp. 1166–1181, Jul. 2018, doi: 10.1109/TUFFC.2018.2834724. [Online]. Available: https://www.ncbi.nlm.nih.gov/pubmed/29993371

[29] A. Swillens, L. Lovstakken, J. Kips, H. Torp, and P. Segers, "Ultrasound simulation of complex flow velocity fields based on computational fluid dynamics," *IEEE Trans. Ultrason., Ferroelectr., Freq. Control*, vol. 56, no. 3, pp. 546–556, Mar. 2009, doi: 10.1109/TUFFC.2009.1071. [Online]. Available: https://www.ncbi.nlm.nih.gov/pubmed/19411213

[30] V. Behar, "Techniques for phase correction in coherent ultrasound imaging systems," *Ultrasonics*, vol. 39, no. 9, pp. 603–610, Aug. 2002.

[31] K. L. Gammelmark and J. Jensen, "2-D tissue motion compensation of synthetic transmit aperture images," *IEEE Trans. Ultrason., Ferroelectr., Freq. Control*, vol. 61, no. 4, pp. 594–610, Apr. 2014, doi: 10.1109/TUFFC.2014.2948.

[32] S. Nikolov, K. Gammelmark, and J. Jensen, "Velocity estimation using recursive ultrasound imaging and spatially encoded signals," in *Proc. IEEE Ultrason. Symp.*, vol. 1, Feb. 2000, pp. 1473–1477.

**Joosje M. K. de Bakker** (Member, IEEE) received the M.Sc. degree in technical medicine, track medical imaging and interventions from the University of Twente, Enschede, The Netherlands, in 2020. She is currently pursuing the Ph.D. degree with the Medical UltraSound Imaging Center (MUSIC), Department of Medical Imaging, Radboud University Medical Center (Radboudumc), Nijmegen, The Netherlands, focusing on ultrafast ultrasound blood velocity vector imaging in the carotid artery.

She carried out her master's thesis at MUSIC, in combination with the Division of Neonatology, Radboudumc, on "Visualization of 2-D Blood Velocity Patterns in the Neonatal Heart Using Ultrafast Ultrasound." Her research interests include ultrafast ultrasound, coded excitation, vector flow imaging, and clinical implementation of this for better personalized treatment.

**Chris L. de Korte** (Fellow, IEEE) received the M.Sc. degree in electrical engineering from the Eindhoven University of Technology, Eindhoven, The Netherlands, in 1993, and the Ph.D. degree in medical sciences from the Thoraxcenter, Erasmus University Rotterdam, Rotterdam, The Netherlands, in 1999, with a focus on intravascular ultrasound elastography.

In 2002, he joined the Clinical Physics Laboratory, Radboud University Medical Center, Nijmegen, The Netherlands, as an Assistant Professor, and became the Head, in 2004. In 2006, he was appointed as Associate Professor of medical ultrasound techniques and he finished his training as a Medical Physicist, in 2007. Since 2012, he has been the Founder and the Director of the Medical UltraSound Imaging Center (MUSIC), Department of Medical Imaging, Radboud University Medical Center (Radboudumc). He was appointed as a Full Professor on Medical Ultrasound Techniques, in 2015. Since 2016, he has been a Full Professor of medical ultrasound imaging with the University of Twente, Enschede, The Netherlands. He has coauthored over 200 peer-reviewed articles in international journals and co-inventor of four patents. His research interests include functional imaging and acoustical tissue characterization for diagnosis, treatment monitoring, and guiding interventions for oncology and vascular applications. Recently, he also focuses on artificial intelligence-driven apps for point-of-care ultrasound.

Dr. de Korte was a recipient of the EUROSON Young Investigator Award 1998 of the European Federation of Societies for Ultrasound in Medicine and Biology.

**Anne E. C. M. Saris** (Member, IEEE) received the M.Sc. degree in medical engineering from the Eindhoven University of Technology, Eindhoven, The Netherlands, in 2012, and the Ph.D. degree from the Radboud University, Nijmegen, The Netherlands, in 2019. She obtained her Ph.D. degree on blood velocity vector imaging in the carotid artery using ultrasound.

She did her Master Graduation Project at the Radboud University Medical Center (Radboudumc), Nijmegen, The Netherlands, on correlation-based discrimination between myocardial tissue and blood in 3-D echocardiographic images, for segmentation purposes. Since 2012, she has been employed by the Medical UltraSound Imaging Center, Radboudumc. Currently, she holds a Tenure Track position. Her research interests include ultrafast ultrasound, 3-D ultrasound imaging, technical development and clinical implementation of ultrasound blood flow imaging, with the overall aim to improve diagnosis, intervention and monitoring of cardiovascular diseases.